Dynamics of a Beta Plane Jet

by

Steven Robert Jayne

Submitted to the Department of Earth, Atmospheric and
Planetary Sciences in partial fulfillment of the
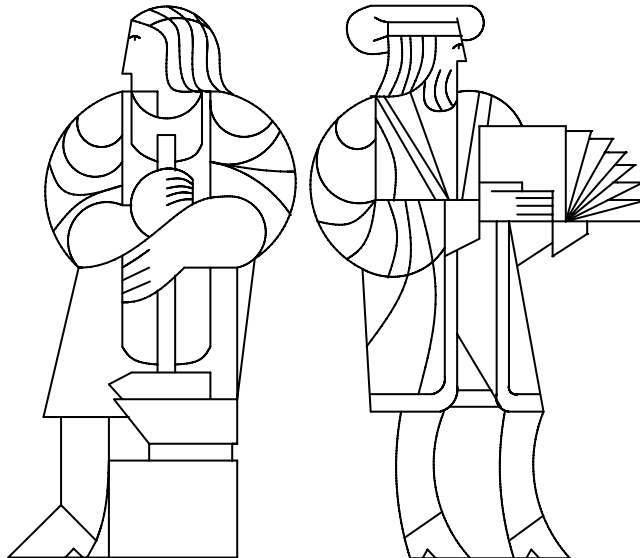requirements for the degree of

Bachelor of Science

at the

MASSACHUSETTS INSTITUTE OF TECHNOLOGY

May 6, 1994

Dynamics of a Beta Plane Jet
by

Steven Robert Jayne

Submitted to the Department of Earth, Atmospheric and Planetary
Sciences on May 6, 1994, in partial fulfillment of the requirements
for the degree of Bachelor of Science

Abstract

The time dependant barotropic vorticity equation was numerically integrated to find the behavior of a prescribed jet on a beta plane. The jet was barotropically unstable and as a result meandered and radiated Rossby waves into the far field. The resulting dynamics were examined for the time mean quantities and the transient eddies. The results of this simple model are remarkably similar to the observational results of Hogg's study of the Gulf Stream (1993). Recirculation gyres were found to form along the jet. We believe the gyres were forced by the rectification of Rossby waves radiated by the meandering jet.

Thesis Supervisor: Paola Malanotte-Rizzoli
Title: Professor of Oceanography

Dedicated to the memory of

Brian D. Collier (1970-1994),

a friend who died too young.

Acknowledgments

I would first like to acknowledge my advisor and friend, Dr. Paola Malanotte-Rizzoli, who over the past four years has help shape my interest in oceanography through her continual support and kindness. It is to Paola that much of the credit belongs for my success and happiness at MIT. I would also like to acknowledge my co-advisor, Dr. Nelson Hogg, whose work and guiding efforts have brought this project to fruition. Together Paola and Nelson have led me through this thesis with suggestions and helpful advice.

I would also like to thank Dr. Roberta Young for always being willing to answer questions about programming and modeling. Dan Goldner provided helpful comments on the draft version of the thesis.

I must acknowledge Chi Phi for providing me with a wonderful house to live in for four years and being family through the thick and thin of MIT life. I would especially like to thank CCA, DDB, EMC, IKC, RAD, MSK, NDL, AP, CSP, BMS, GGS and AMV. I would also like to thank the friends I've had through my first four years here, especially, LIA, MLD, FGH, AKH, SMH, EBK, CW, ERW and DW. All you have filled my four years with happiness.

I would like to thank my Mom and Dad for their 21 years of support and giving me the opportunity to come to MIT.

Table of Contents

Chapter 1

Introduction

Recirculation occurs in many observed oceanographic systems and is reproduced by the general circulation models relevant to those systems as well. The Gulf Stream Recirculation Gyres are a prime example of this phenomenon. The transport of the Gulf Stream as it leaves the continental slope at Cape Hatteras has a transport of approximately 65 Sverdrups (1 Sverdrup = 10^6 m^{3}s^{-1}; hereafter Sv.). When the stream reaches the New England Sea Mounts at 65° W, the transport of the system has increased to 150 Sv. (Hogg, 1992). This increase in the total circulation of the Gulf Stream system is primarily due to the additional transport of the recirculation gyres north and south of the stream. The strength of the recirculation is several times what could be expected from the wind or buoyancy forcing alone (Hogg, 1992).
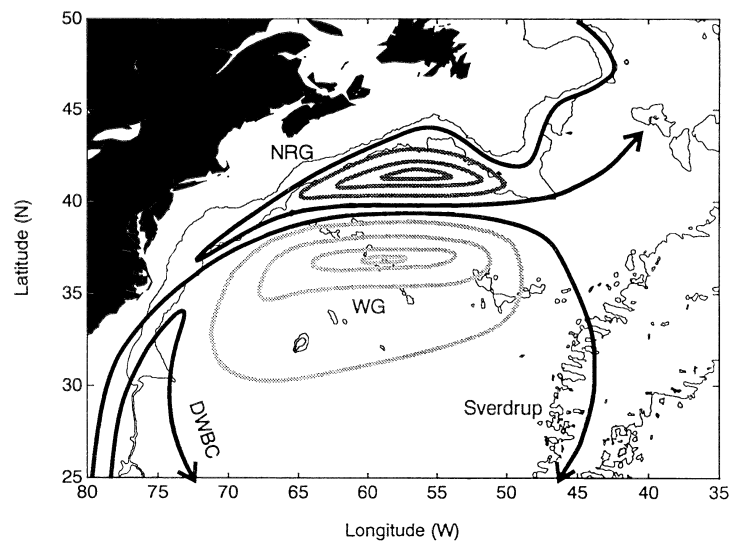

Figure 1.1: Scheme for recirculation in the Gulf Stream system. Heavy lines are streamlines. To the north of the stream is the Northern Recirculation Gyre (NRG) carrying 40-60 Sv. and to the south of the stream is the "Worthington Gyre" (WG) also carrying 40-60 Sv. (Hogg, 1992).

Recirculation is also seen in the wind forced, quasi-geostrophic, basin scale models. The gyres are generally pressed along the zero wind stress curl line (Holland and Rhines, 1980). The question of what drives this recirculation in both the real world and in numerical simulations has not been adequately resolved.

Two significant theories have been put forth to explain the observed recirculation. First, inertial theories conclude that the recirculation is driven by advection of relative vorticity by the western boundary current or by injection of baroclinic stretching of the layers (Fofonoff, 1954; Hogg and Stommel, 1985; Marshall and Nurser, 1986; Cessi 1990). Alternatively is the theory that the rectification of eddies results in a mean recirculation (Hogg, 1988; Hogg, 1993; Malanotte-Rizzoli *et al.*, submitted). The latter theory will be the primary stimulus for this work.

There exists a rich eddy field in the Northwest Atlantic having a kinetic energy maximum at the climatological axis of the Gulf Stream. The eddy field decays rapidly away from the jet. Explanations for the eddy field generally depend upon the meandering of the Gulf Stream as a the source of the energy (Hogg, 1988; Malanotte-Rizzoli *et al.*, submitted). The eddy field fluxes potential vorticity, which can be related to a mean circulation by the mean potential vorticity balance. We derive this relation from the conservation of potential vorticity; $\frac{dq}{dt} = 0$. Translating this into an Eulerian frame has a full time derivative of

$$\frac{\partial q}{\partial t} + \boldsymbol{u} \cdot \nabla q = 0 \tag{1.1}$$

where $\mathbf{u} = [u, v]$ is the horizontal velocity vector and q is the potential vorticity. Decomposing $\boldsymbol{u}$ and q into a time mean and time varying quantity yields $\mathbf{u}(t) = \bar{\mathbf{u}} + \mathbf{u}'(t)$ and $q(t) = \bar{q} + q'(t)$. The overbar represents the time mean and the prime the deviation from it. The time means of the random eddy field being zero, thus, $\bar{u}' = 0$ and $\bar{q}' = 0$. This

expands the equation into 6 pieces:

$$\frac{\partial \bar{q}}{\partial t} + \frac{\partial q'}{\partial t} + \bar{\boldsymbol{u}} \cdot \nabla \bar{q} + \boldsymbol{u}' \cdot \nabla \bar{q} + \bar{\boldsymbol{u}} \cdot \nabla q' + \boldsymbol{u}' \cdot \nabla q' \; = \; 0 \tag{1.2}$$

The first term, $\frac{\partial \bar{q}}{\partial t} = 0$, since the time derivative of the mean field is 0, by definition. Taking the time mean of the remaining equation removes the $\frac{\partial q'}{\partial t}$, $\boldsymbol{u}' \cdot \nabla \bar{q}$ and $\bar{\boldsymbol{u}} \cdot \nabla q'$. This reduces equation (1.2) to:

$$\overline{\bar{\boldsymbol{u}} \cdot \nabla \bar{q}} + \overline{\boldsymbol{u}' \cdot \nabla q'} \; = \; 0 \tag{1.3}$$

We can further express $\overline{\boldsymbol{u}' \cdot \nabla q'} = \nabla \cdot \overline{(\boldsymbol{u}' \cdot q')} - \overline{q'(\nabla \cdot \boldsymbol{u}')}$, where $\overline{q'(\nabla \cdot \boldsymbol{u}')} = 0$ by the assumption of non-divergent flow. The mean of a mean quantity is simply the mean quantity itself, therefore equation (1.3) is reduced to:

$$\bar{\boldsymbol{u}} \cdot \nabla \bar{q} \; = \; -\nabla \cdot \overline{(\boldsymbol{u}' \cdot q')} \tag{1.4}$$

Therefore, the divergence of the eddy vorticity flux can force a mean circulation.

Hogg (1993) showed that the mean circulation driven by the vorticity flux could be obtained analytically through a modified Sverdrup relation. This can be seen using the linearized barotropic vorticity equation on a beta plane, namely a modified Sverdrup balance. To first order the deep northern recirculation gyre is barotropic (Schmitz, 1980; Richardson, 1985; Hogg, 1993). Starting with the conservation of potential vorticity equation and breaking the potential vorticity into its components yields:

$$\frac{dq}{dt} \; = \; \frac{d}{dt}(\frac{\zeta + f}{H}) \; = \; \frac{\partial \zeta}{\partial t} + \boldsymbol{u} \cdot \nabla \; (\frac{\zeta + f}{H}) = 0 \tag{1.5}$$

where ζ is the relative vorticity, f is the planetary vorticity, H is the depth and $\boldsymbol{u}$ is again the horizontal velocity vector. In quasi-geostrophy, the relative vorticity is related to the streamfunction by; $\zeta = \nabla^2 \psi$, and the velocity vector is defined by $\boldsymbol{u} = [u, v] = \left[-\frac{\partial}{\partial y}, \frac{\partial}{\partial x}\right]\psi$. In the beta plane approximation, $f = f_0 + \beta y$, where, for mid-

latitudes, such as where the Gulf Stream is found, $f_0 \approx 9.76 \times 10^{-5} \, (s)^{-1}$ and $\beta \approx 2 \times 10^{-11} \, (ms)^{-1}$. Also, neglecting topography and assuming that there is no dissipation, we have the barotropic vorticity equation for a flat bottomed, inviscid, homogeneous ocean.

$$\frac{\partial}{\partial t}\nabla^2 \, \psi + J\left(\psi, \nabla^2 \, \psi + \beta y\right) = 0 \tag{1.6}$$

Where $J()$ is the determinant of the Jacobian matrix, $J(A, B) = \frac{\partial A}{\partial x} \cdot \frac{\partial B}{\partial y} - \frac{\partial A}{\partial y} \cdot \frac{\partial B}{\partial x}$.

Reworking the mean vorticity equation, (1.4), in this form yields:

$$J\left(\overline{\psi}, \nabla^2 \, \overline{\psi} + \beta y\right) = -\overline{J\left(\psi', \nabla^2 \, \psi'\right)} \tag{1.7}$$

Further linearization of this equation yields

$$\beta\frac{d\psi}{dx} = -\overline{J\left(\psi', \nabla^2 \, \psi'\right)} \tag{1.8}$$

or rewritten in terms of the velocity vector and potential vorticity:

$$\beta v = -\nabla \, \overline{(\boldsymbol{u'} \cdot q')} \tag{1.9}$$

Which is the linearized version of (1.4). Integration to find the depth averaged zonal velocity yields:

$$\beta V = \frac{1}{D}\int_{-D}^{0} -\nabla \, \overline{(\boldsymbol{u'} \cdot q')} \, dz \tag{1.10}$$

where D is the ocean depth and $[U, V] = \frac{1}{D}\int_{-D}^{0} [u, v] \, dz$. This is the modified Sverdrup relation. Hogg (1993) calculated a recirculation of 30-40 Sv. for each of the Gulf Stream recirculation gyres from the measurements collected at the SYNOP experiment array.

As a heuristic argument, we consider a ψ' modeled as $\langle\psi'^2\rangle = C^2 e^{-2\left(\frac{x}{L_x}\right)^2 - 2\left(\frac{y}{L_y}\right)^2}$ with length scales, L_x and L_y, and strength, C, as an approximation to the observed Gulf Stream eddy field. This is motivated by Hogg's study of the Gulf Stream (1993). Solving (1.10) where $L_x = 6 \times 10^5 m$, $L_y = 2 \times 10^5 m$ and $C = 3.4 \times 10^4\,(m^2 s^{-1})$, which were estimated from Hogg (1993), we find 2 counter-rotating gyres are created as seen in figure 1.2.

Linear Solution

CONTOUR FROM −7500 TO 7500 BY 500
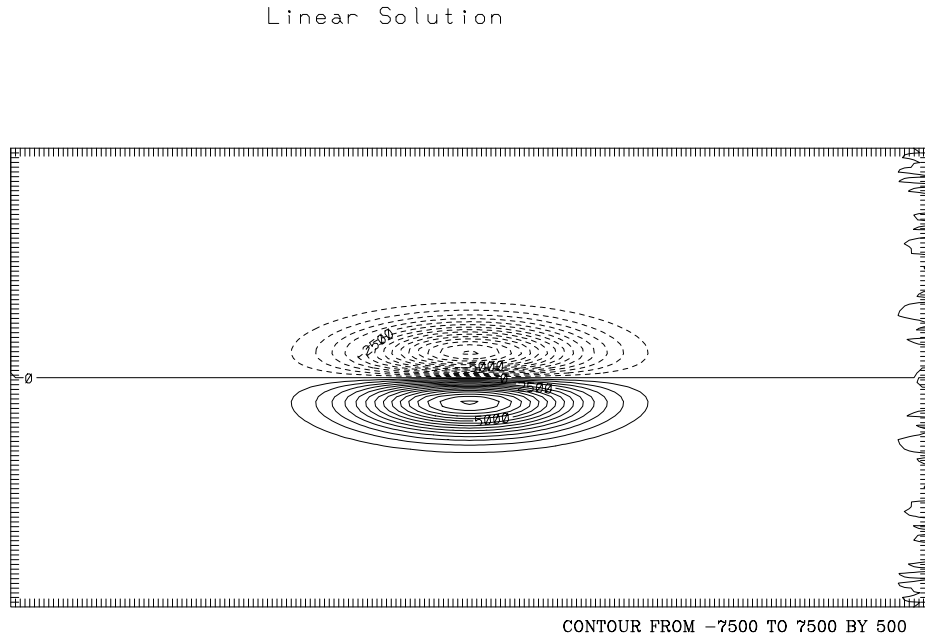
Figure 1.2: Solution to (1.10) forced by model eddy streamfunction, showing 2 counter rotating gyres, each carrying 35 Sv.

We further extended these results by time integrating to a steady state the fully nonlinear barotropic vorticity equation, (1.7), using a numerical model, which will be discussed more fully in the following chapter. Forcing the model with the same $\langle\psi'^2\rangle$ as in figure 1.2 results in the steady state solution shown in figure 1.3.
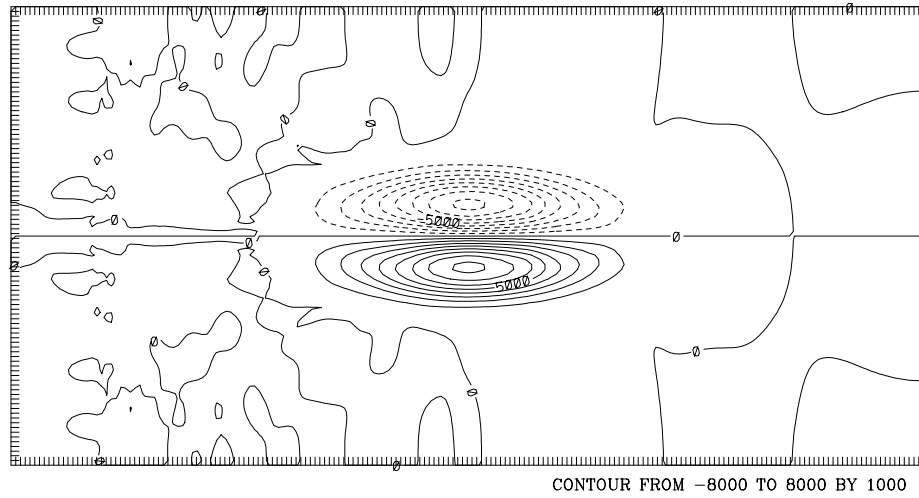
CONTOUR FROM −8000 TO 8000 BY 1000

Figure 1.3: Steady State of the model forced with a divergence of an eddy flux, again showing two counter rotating gyres, each carrying 40 Sv.

The nonlinear terms contribute an additional 10% to the total circulation over that expected from the linear Sverdrup balance and do not create significant changes in the morphology of the gyres.

Chapter 2

Formulation of the Barotropic Model

The barotropic vorticity equation simply states that the potential vorticity of a parcel is conserved in the absence of forcing and dissipation. However, dynamically and mathematically it is a very complex equation. As it has no general analytical solutions, a numerical model was written to approximately solve the time dependent nonlinear partial differential equation. Using finite difference methods, the equation was evaluated on a uniform grid with a spacing of 18.75 km. The resolution of the model was chosen to be less than 20 km, in order to resolve baroclinic eddies. (Even though we are dealing with a barotropic model, we shall extend this work to the baroclinic case.) The total size of the basin was 3600 km in the zonal direction by 1800 km in the meridional direction, chosen to provide adequate space for the jet to meander and allow radiation from the jet to propagate away from it before encountering a boundary. The model was stepped forward in time, solving for the vorticity, ζ, and inverting to find the streamfunction, ψ, at every time step. In finite difference form, using Euler's method as the prototypical example, the equation becomes:

$$\zeta_{t+1} = \zeta_t - \Delta t \times J(\psi_t, \zeta_t + \beta y) \tag{2.1}$$

A standard Laplacian inverter was used to find ψ from the relation $\zeta = \nabla^2 \psi$, using the Generalized Buneman Algorithm (Adams *et al.*, 1988). The three-point centered first derivatives were use for the velocity vector, $u = [u, v] = \left[-\frac{\partial}{\partial y}, \frac{\partial}{\partial x}\right]\psi$. The five-point centered Laplacian was used for $\zeta = \nabla^2 \psi$ and the standard Arakawa Jacobian was for the advection of vorticity term, $J(\psi, \zeta)$ (Arakawa, 1966). The time integration was performed using a combination of Leapfrog and Euler backward time stepping. We found that 10 leapfrogs followed by 10 Euler backwards steps was the most stable. Other time stepping

methods were tried in the search for a stable scheme, including Euler forward, which is intrinsically unstable; Leapfrog by itself, as well as the Adams-Bashford method and Leapfrog Backward. have an instability called computational mode. The computational mode arises from the use of three time step levels (t-1, t, and t+1) involved with Leapfrog, Adams-Bashford and Leapfrog Backward. The Euler backward step only use two time levels (t and t+1) and thus eliminates the computational mode. By using a combination of Leapfrog and Euler backward, computation time is saved over using the Euler backward step exclusively, as the Euler backward is twice as computationally expensive as the Leapfrog step due to the calculation of the predictor-corrector step in Euler backward (Haltiner and Williams, 1980).

Sponges were added at the eastern and western boundaries to absorb excited Rossby waves. The sponges act as a dissipation term, $-A_H \nabla^2 \psi$, on the right hand side of the equation (1.6). The strength of the sponges was an adjustable parameter of the model. Varying the strength of the sponges had strong effects on the dynamics of the interior of the computational domain. We will quantify the effect of the sponges in Chapter 4.

To find the solution for the recirculation seen in figure 1.2, the model was forced by the divergence of the eddy vorticity flux, where $\psi' = Ce^{-(\frac{x}{L_x})^2 - (\frac{y}{L_y})^2}$ as discussed previously, and $\psi = 0$ was set as the boundary condition for the inverter, and the model was time stepped to until it reached a steady state.

To establish the validity of the model, we used as a test the results of Flierl, Malanotte-Rizzoli and Zabusky (1987) with a zonally periodic version of the model. No sponges were used and a zonal jet was imposed as an initial condition. The primary results were that jet meanders grew to finite amplitude with a wavelength determined by the initial disturbance and the growth is strongly dependent on beta. For $\beta = 0$ the axis of the jet breaks and paired vortices result.

Barotropic instability is the driving force behind the meandering of the model jet and production of wave radiation from the jet. Instability occurs when the north-south cross section of potential vorticity has local extrema. This implies that the meridional derivative of potential vorticity has zeros, $\left.\frac{\partial q}{\partial y}\right|_{y_c} = 0$. Decomposing the potential vorticity into its components yields:

$$\left.\frac{\partial \zeta}{\partial y}\right|_{y_c} + \beta = 0 \tag{2.2}$$

Considering a zonal jet, where $\psi = \psi(y)$, and $\zeta = \nabla^2 \psi$ gives us

$$\left.\frac{\partial^3 \psi}{\partial y^3}\right|_{y_c} + \beta = 0 \tag{2.3}$$

which can be rewritten in terms of the velocity as:

$$\beta - \left.\frac{\partial^2 u}{\partial y^2}\right|_{y_c} = 0 \tag{2.4}$$

Even though (2.4) is only a necessary condition for instability, the model showed that the imposed jet was unstable for the physical parameter range.

Chapter 3

Results from the Barotropic Model

A jet modeled as an error function was imposed as a boundary condition, where the streamfunction at the east and west boundaries is given by:

$$\psi(y) = -(S)\,erf(\frac{y}{L}) \tag{3.1}$$

where S is the strength of the jet and L is the half width of the jet. The half width and the strength of the jet were parameters of the model. The model domain was initialized with the jet plus random noise to seed instabilities. The imposed jet in this model is barotropically unstable for most L within the physical range of interest. The model was run for varying strengths of jets and varying sponge strengths. We will first concern ourselves with the aspects of a single model run in order to discuss dynamics that were seen in all of the model runs. The parameters for this run was a jet streamfunction strength of 50,000 m^2s^{-1} which translates in a 5000 m deep ocean to a barotropic transport of 500 Sv. The half width was set at 50 km, which gives a maximum zonal velocity, u, of 1.078 ms^{-1}. This unphysical transport is necessary to reproduce jet speeds, and consequently the dynamics seen in the ocean, but it is clearly a limitation of a barotropic model. The initial jet is shown in figure 3.1.

New PSI at time   0.

CONTOUR FROM -45000 TO 45000 BY 5000
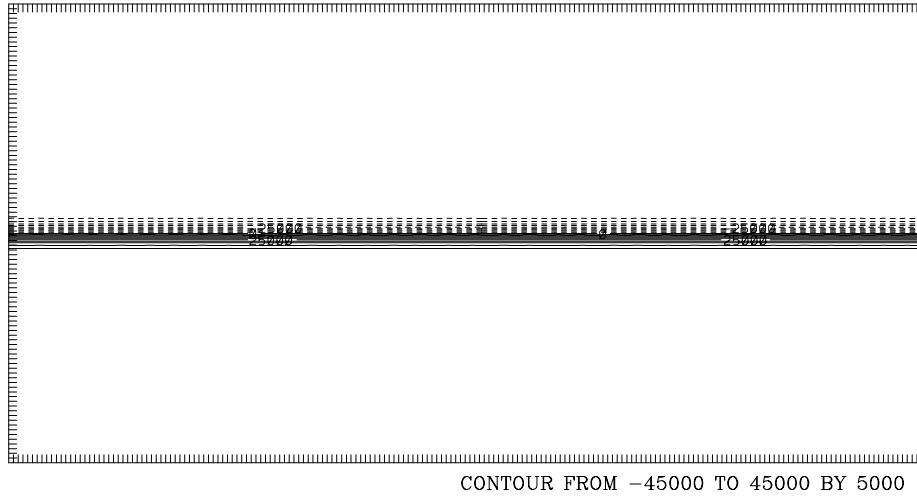
Figure 3.1: Initial streamfunction for model run

The corresponding potential vorticity contour plot is shown in figure 3.2 and north-south cross section through the middle of domain is shown in figure 3.3. Note that there are inversions in the potential vorticity showing that the jet is barotropically unstable.
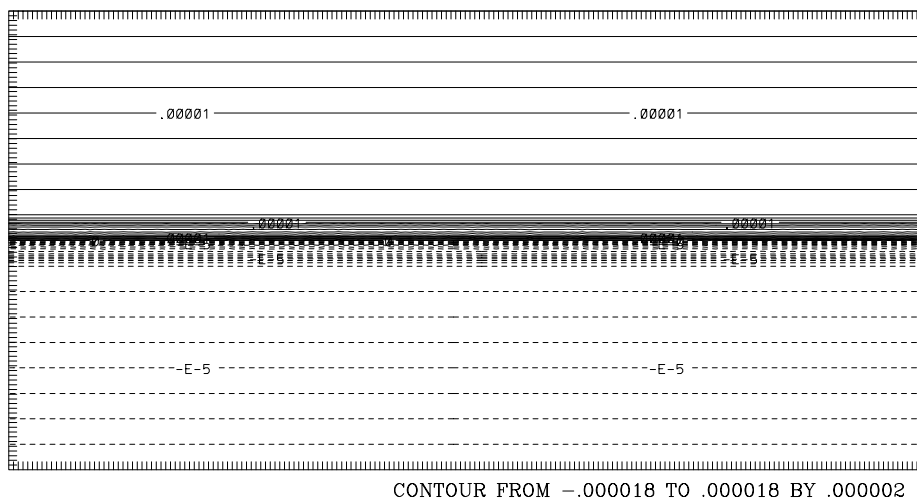
Potential Vorticity at time   0.

CONTOUR FROM -.000018 TO .000018 BY .000002

Figure 3.2: Initial potential vorticity distribution for model run
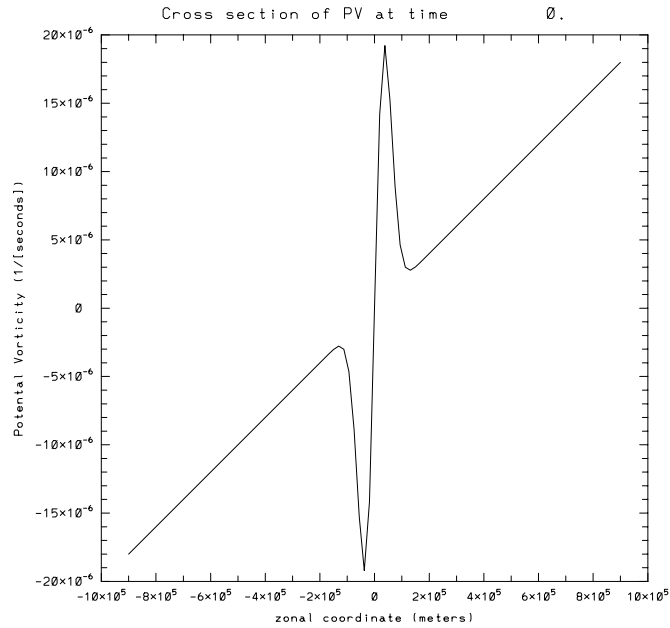
Figure 3.3: Cross section of potential vorticity for initial jet with local extrema

The model was time stepped for the equivalent of 20 years and the final field is the snapshot of ψ, shown in figure 3.4, with a corresponding potential vorticity plot and cross section in figures 3.5 and 3.6. Clearly the jet shows large meanders and a very rich eddy field has developed around the jet. The potential vorticity shows that there has been a cascade to quasi-geostrophic turbulence.

New PSI at time 640000000.

CONTOUR FROM −80000 TO 120000 BY 10000
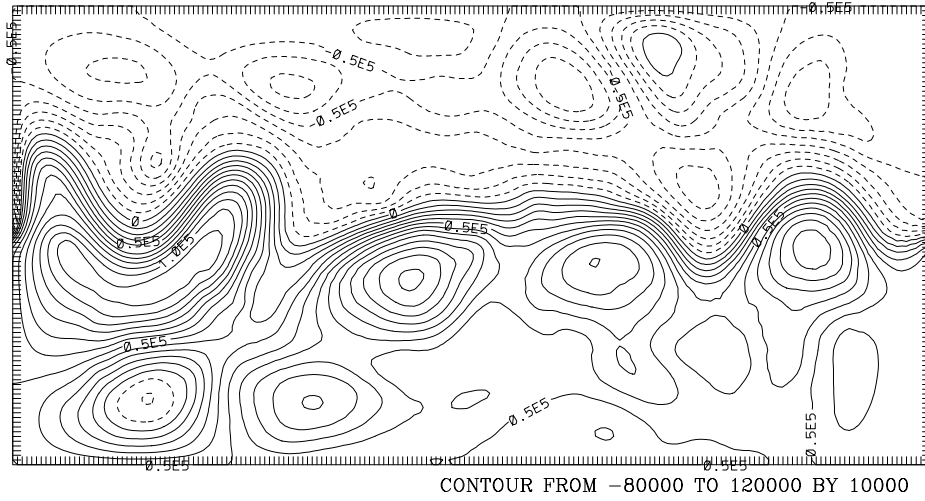
Figure 3.4: Instantaneous plot of the streamfunction after 20 years of integration

Potential Vorticity at time 640000000.

CONTOUR FROM −.00003 TO .0000225 BY .0000025
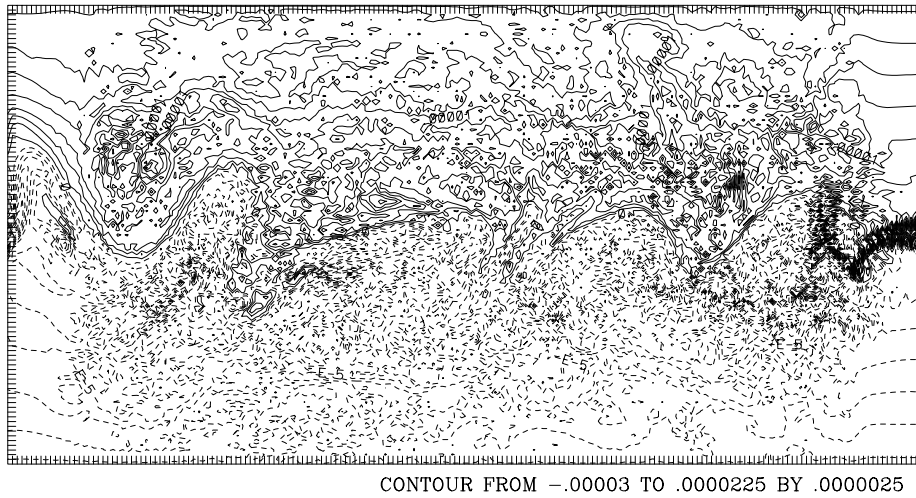
Figure 3.5: Potential vorticity distribution after 20 years of integration
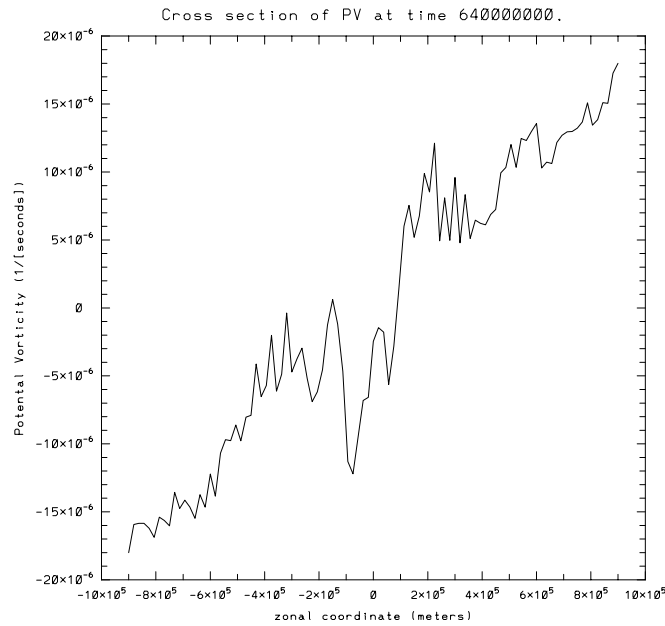
Figure 3.6: North-South cross section of potential vorticity after 20 years of integration

By monitoring a single point in the model, we can gain some information about the wave spectrum characterizing that point over time. We therefore recorded ψ at a point in the lower left quadrant away from the wall and away from the sponge layers. A plot of the streamfunction at the point is shown in figure 3.7.
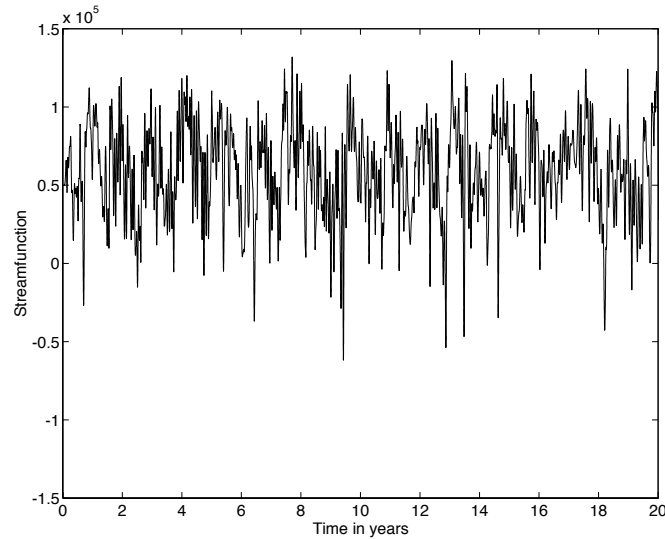
Figure 3.7: Streamfunction as a function of time at a point in the model

The energy spectrum of the ψ at the point was evaluated using MATLAB's spectrum function. Only a broadband spectrum was found as figure 3.8 shows. There are no strong peaks in the energy at any particular frequency which would indicate a signal.
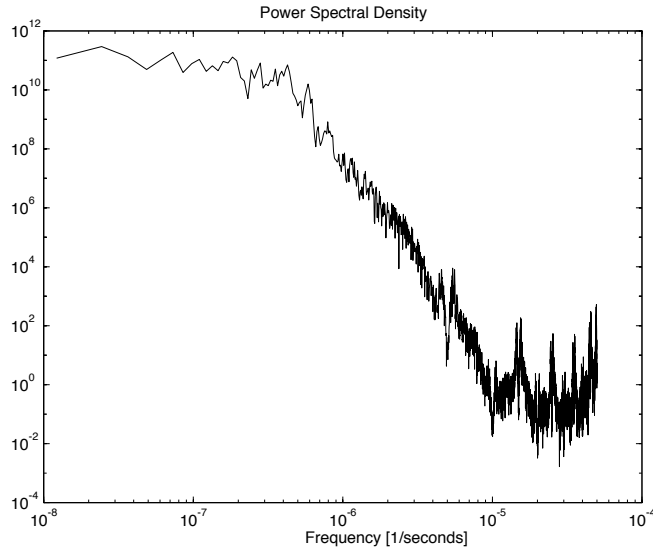
Figure 3.8: Spectral decomposition of wave energy

Time averaged fields for ψ and q were taken for the last 10 years of the run. The resulting mean fields are shown in figures 3.9 and 3.10 and a cross section of potential vorticity is seen in 3.11. We see in the time mean of ψ large counter-rotating recirculation gyres corresponding to areas of homogeneous potential vorticity found to the north and south of the jet. We shall discuss the length scales and number of these recirculation gyres in the next chapter.
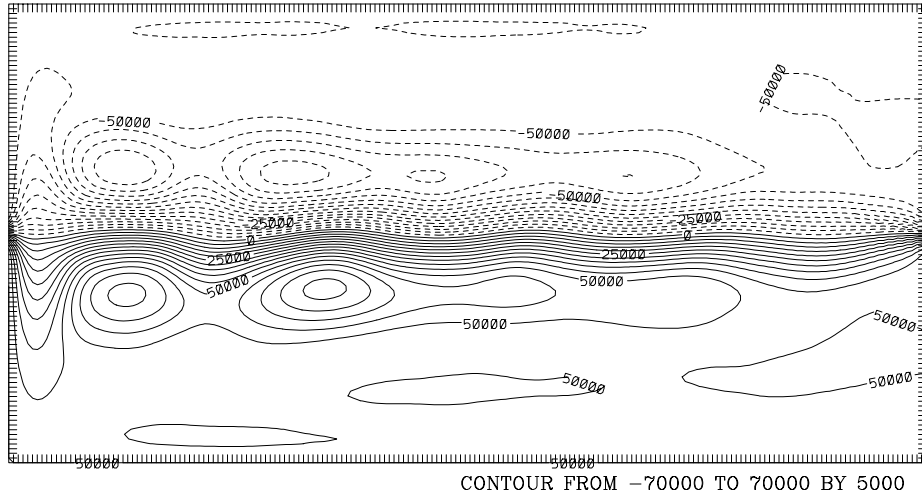
New PSI at time   32000.

CONTOUR FROM −70000 TO 70000 BY 5000

Figure 3.9: Mean streamfunction for last 10 years of model run, the most prominent feature is the large recirculation patterns to the North and South of the jet.
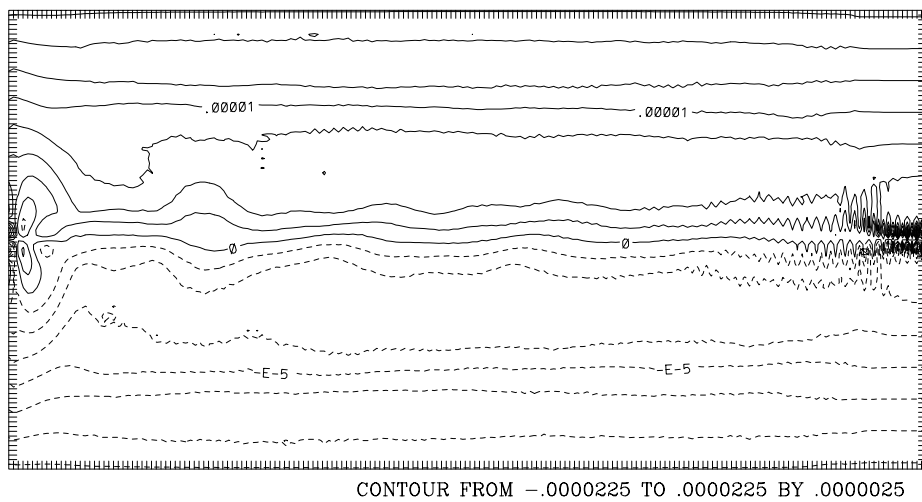
Potential Vorticity at time   32000.

CONTOUR FROM −.0000225 TO .0000225 BY .0000025

Figure 3.10: Mean potential vorticity for last 10 years of model run, note the large areas of homogeneous potential vorticity
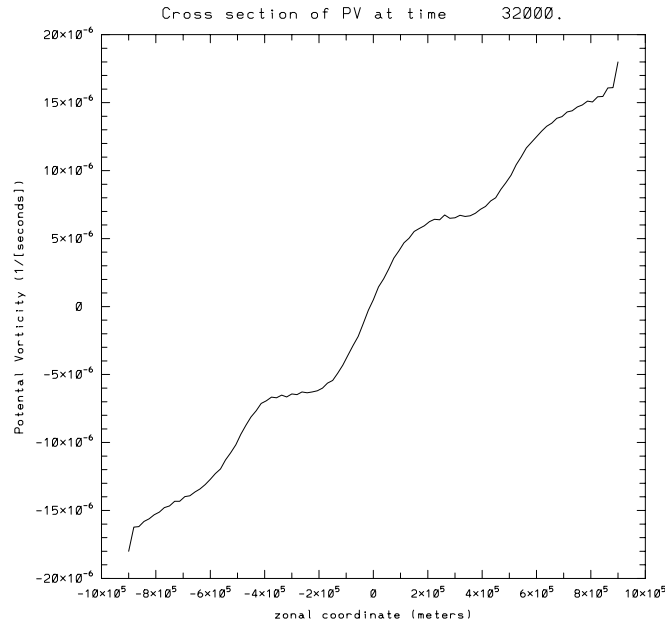
Figure 3.11: North-South cross section of potential vorticity showing shelves of homogenous potential vorticity.

If we scatter plot the mean ψ versus the mean q, for the model domain, we obtain figure 3.12. We can see 3 distinct areas on the curve. The first is the two horizontal regions where ψ is changing, but q is not. These represent the areas of recirculation where the potential vorticity is homogenized. The second area is the two vertical strips where q is changing, but ψ is constant. These areas of quiescent fluid where the change in the potential vorticity is due to the βy planetary gradient. The third and largest feature is the large sloping area with a $\frac{\partial q}{\partial \psi} = -1.1 \times 10^{-10}$ which is the change in ψ and q across the mean jet.
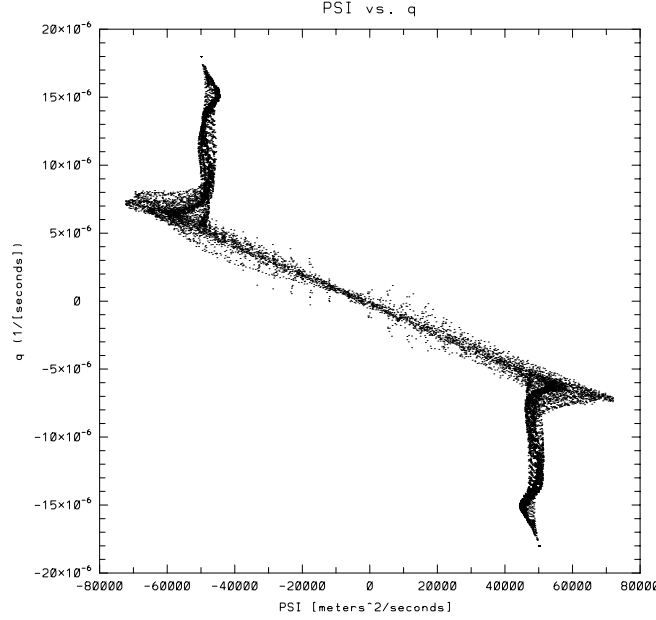
Figure 3.12: Mean streamfunction, ψ, vs. mean potential vorticity, q.

We calculated the time mean of the Reynolds' stress fields, $\overline{u' \cdot u'}$, $\overline{u' \cdot v'}$ and $\overline{v' \cdot v'}$, as well as $\overline{u' \cdot q'}$, $\overline{v' \cdot q'}$ and $\overline{\psi' \cdot \psi'}$ over the last 10 years of the model run. The calculation of these fields relies on the following argument. First we decompose ψ into a mean and time varying part:

$$\psi(t) = \overline{\psi} + \psi'(t) \tag{3.1}$$

Therefore:

$$\psi \cdot \psi = \overline{\psi} \cdot \overline{\psi} + \overline{\psi} \cdot \psi' + \psi' \cdot \overline{\psi} + \psi' \cdot \psi' \tag{3.2}$$

Taking the time mean of (3.2) yields:

$$\overline{\psi \cdot \psi} = \overline{\overline{\psi} \cdot \overline{\psi}} + \overline{\overline{\psi} \cdot \psi'} + \overline{\psi' \cdot \overline{\psi}} + \overline{\psi' \cdot \psi'} \tag{3.3}$$

However, $\overline{\overline{\psi} \cdot \psi'} = \overline{\psi' \cdot \overline{\psi}} = 0$ and $\overline{\overline{\psi} \cdot \overline{\psi}} = \overline{\psi} \cdot \overline{\psi}$, by similar argument as in equation (1.2), leaving us with:

$$\overline{\psi \cdot \psi} \;=\; \overline{\psi} \cdot \overline{\psi} + \overline{\psi' \cdot \psi'} \tag{3.4}$$

Rearranging gives us:

$$\overline{\psi' \cdot \psi'} \;=\; \overline{\psi \cdot \psi} - \overline{\psi} \cdot \overline{\psi} \tag{3.5}$$

Therefore, by averaging the product field of every time step and then subtracting the product of the mean fields yields the mean product of the time varying fields. Figures 3.13 through 3.23 show the mean of the time varying fields and North-South cross sections through them at 3 different zonal locations separated by 131.25 km. The cross sections are denoted by vertical lines labeled 'A', 'B' and 'C' on the contour plots, and by similar line labels on the cross sections.
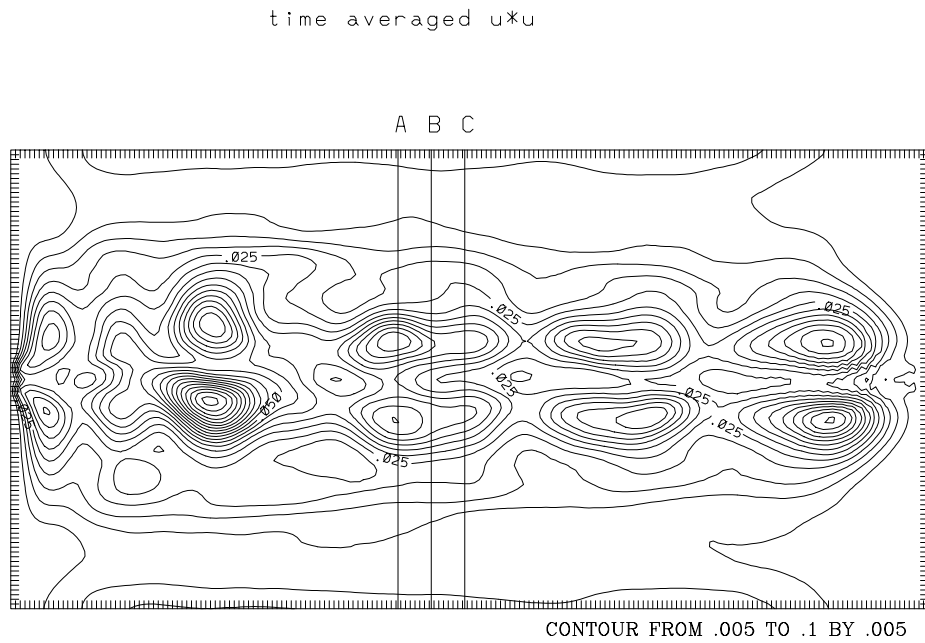
A B C

CONTOUR FROM .005 TO .1 BY .005
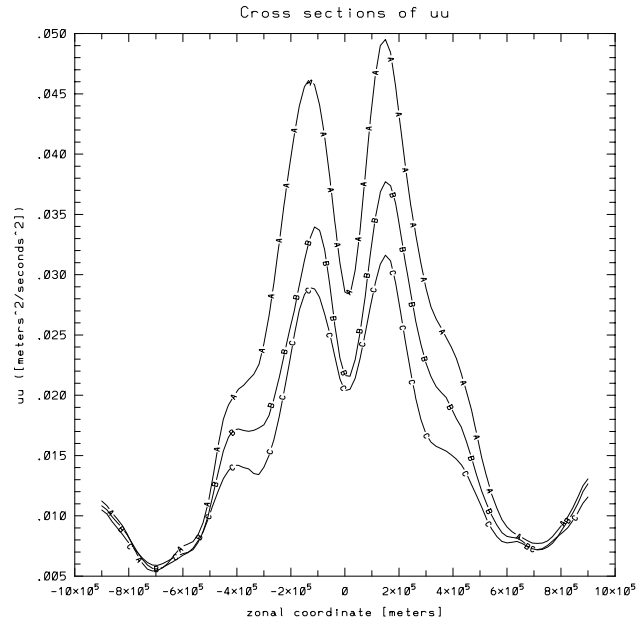
Figure 3.13: $\overline{u' \cdot u'}$

Cross sections of uu

uu ([meters^2/seconds^2])

zonal coordinate [meters]

Figure 3.14: North-South cross sections of $\overline{u' \cdot u'}$

28

time averaged u*v

A B C

CONTOUR FROM −.08 TO .09 BY .01

Figure 3.15: $\overline{u' \cdot v'}$
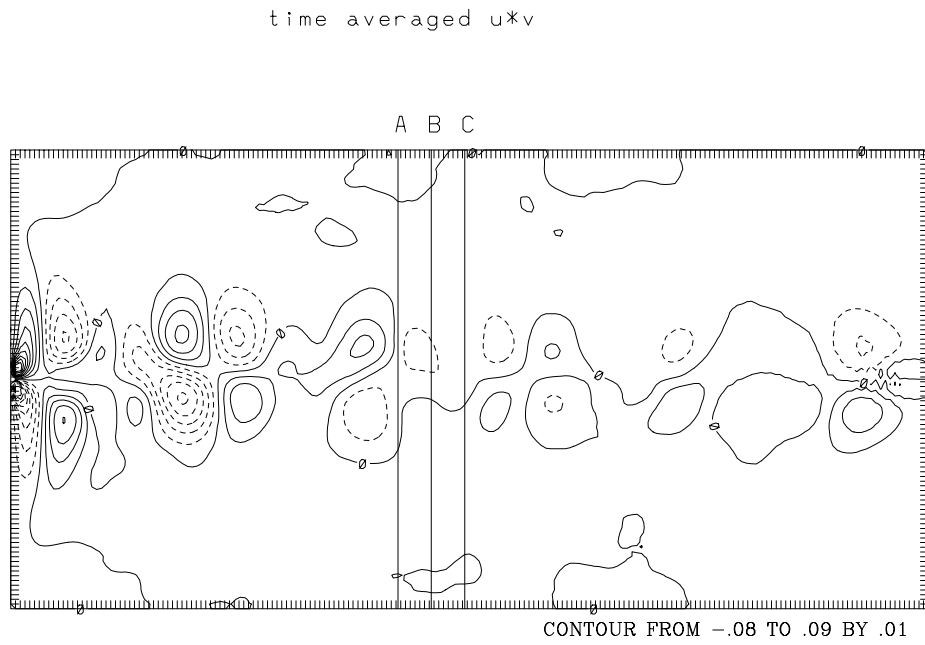
Cross sections of uv
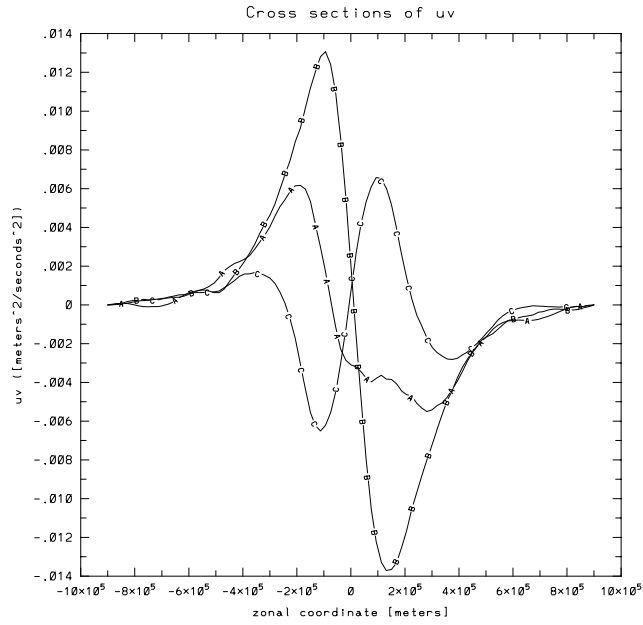
Figure 3.16: North-South cross sections of $\overline{u' \cdot v'}$

time averaged v*v

A B C

CONTOUR FROM .05 TO 1.2 BY .05

Figure 3.17: $\overline{v' \cdot v'}$

Cross sections of vv

vv ([meters^2/seconds^2])

zonal coordinate [meters]
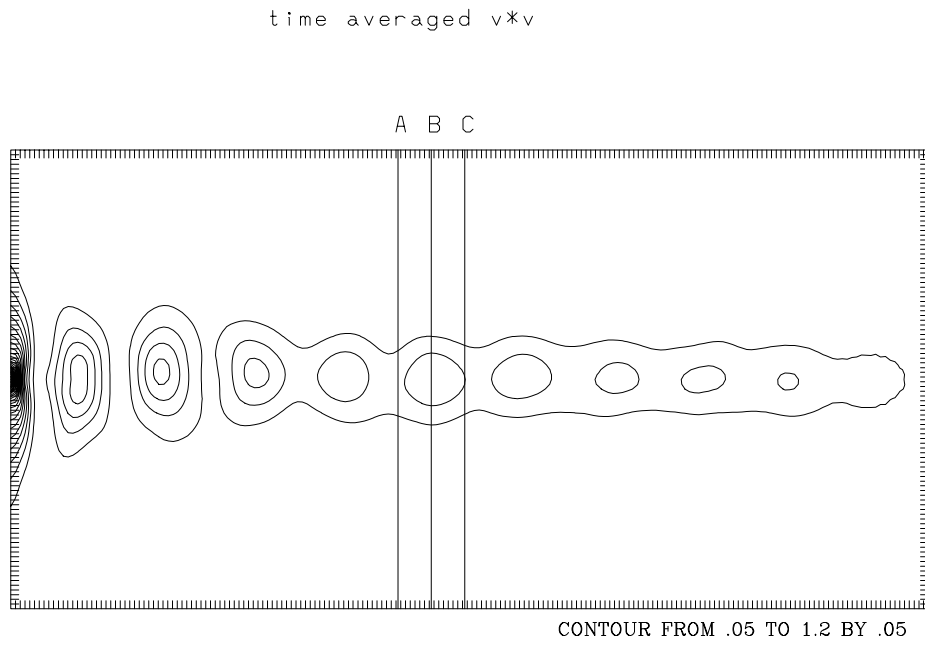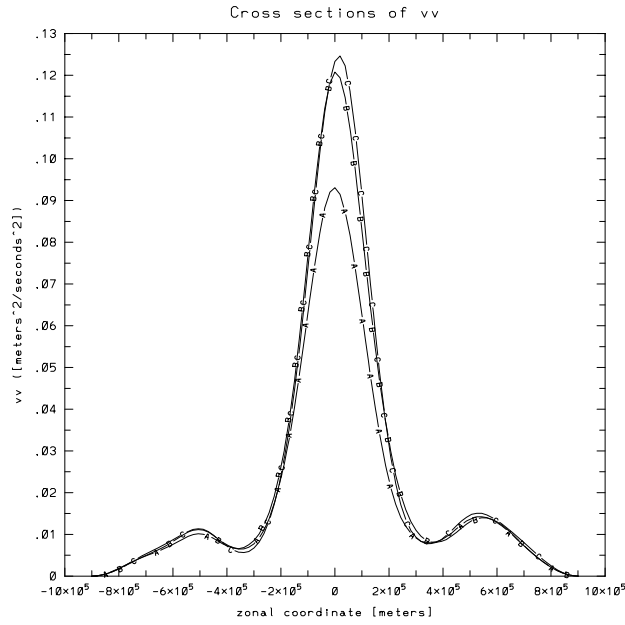
Figure 3.18: North-South cross sections of $\overline{v' \cdot v'}$

time averaged u*q

A B C

CONTOUR FROM −.0000013 TO .0000013 BY .0000001

Figure 3.19: $\overline{u' \cdot q'}$
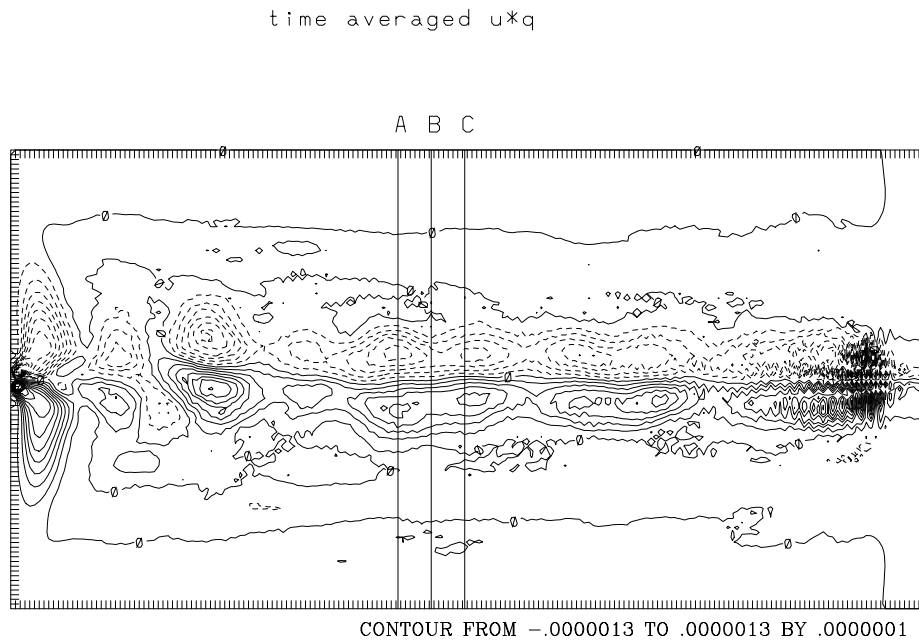
Cross sections of uq
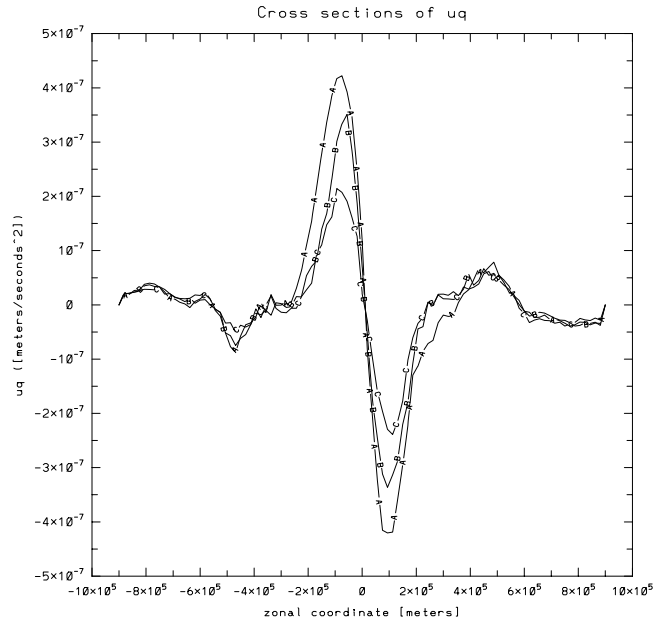
Figure 3.20: North-South cross sections of $\overline{u' \cdot q'}$

time averaged v*q

A B C

CONTOUR FROM −.000019 TO .000002 BY .000001

Figure 3.21: $\overline{v' \cdot q'}$

Cross sections of vq

zonal coordinate [meters]
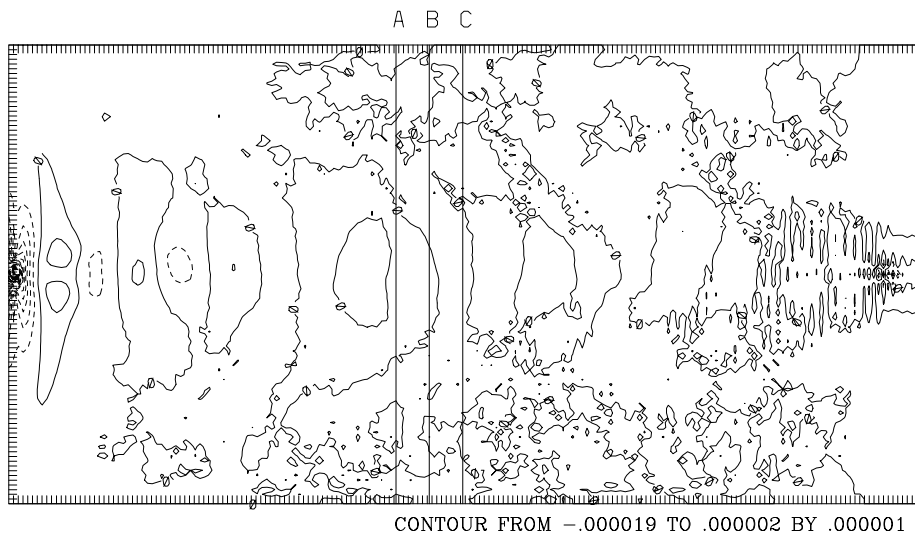
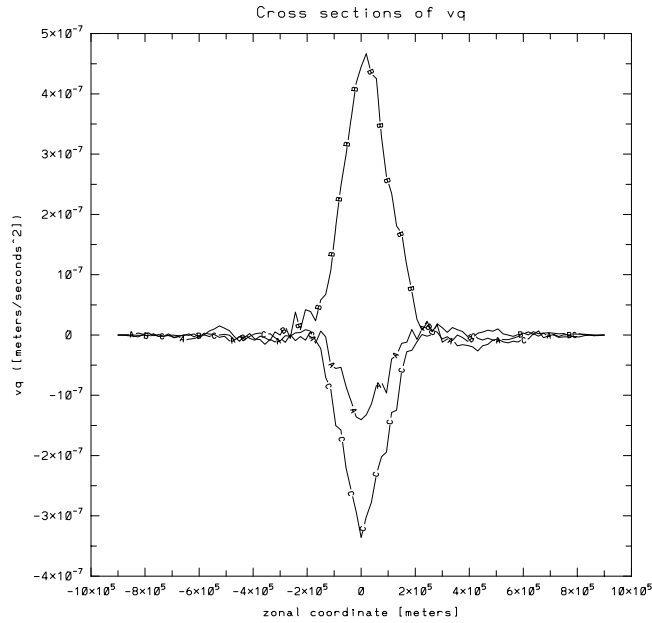**Figure 3.22:** North-South cross sections of $\overline{v' \cdot q'}$

Again we consider equation (1.10), which is the modified Sverdrup balance. Taking the divergence of the measured eddy vorticity flux (figure 3.23) and integrating yields figure 3.24.
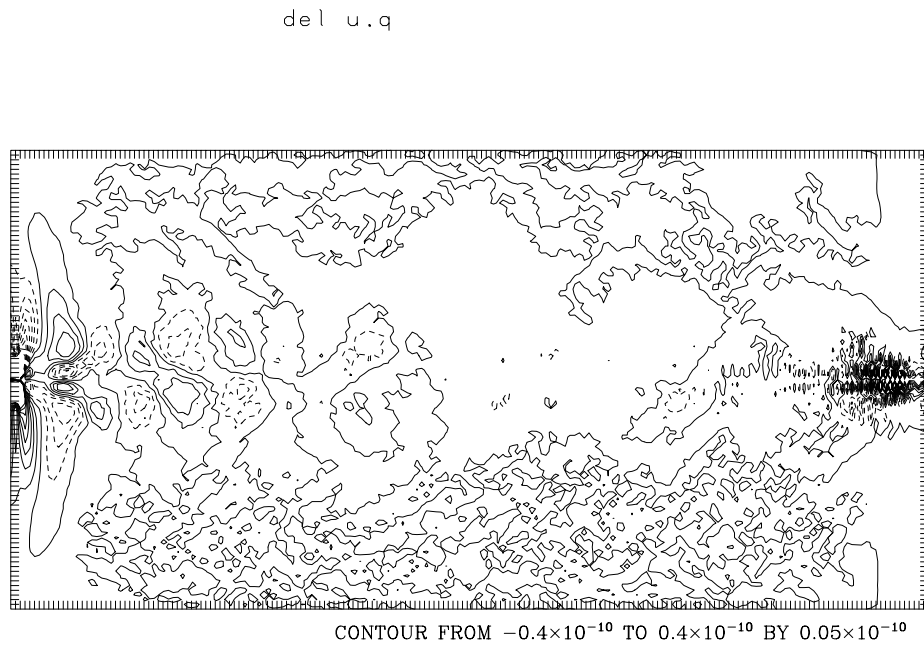
del u.q

CONTOUR FROM -0.4×10^{-10} TO 0.4×10^{-10} BY 0.05×10^{-10}

Figure 3.23: $\nabla \cdot \overline{(\mathbf{u'} \cdot q')}$
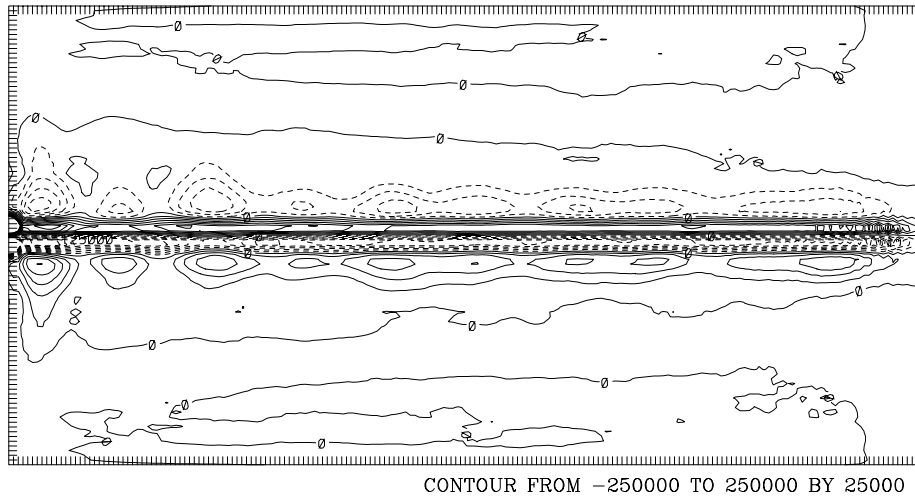
CONTOUR FROM −250000 TO 250000 BY 25000

Figure 3.24: The recirculation predicted by the modified Sverdrup balance

Figure 3.24 shows that a recirculation of counter-rotating gyres to the north and south of the stream is predicted by equation (1.10). Each of the outside recirculation gyres carries approximately 375 Sv. (for a 5000 m barotropic ocean), therefore total system carries 2.5 times the jet's transport. However, we note that there is an inner anticyclonic circulation trapped near the stream, the cause for which is unknown. It is possibly an artifact of the numerical integration or, more likely, of using the linearized equation in a region that is probably very strongly nonlinear. Alternatively, it may be induced by the divergence of the Reynolds' stresses of trapped-trapped wave interactions over a flat bottom (Malanotte-Rizzoli, submitted).
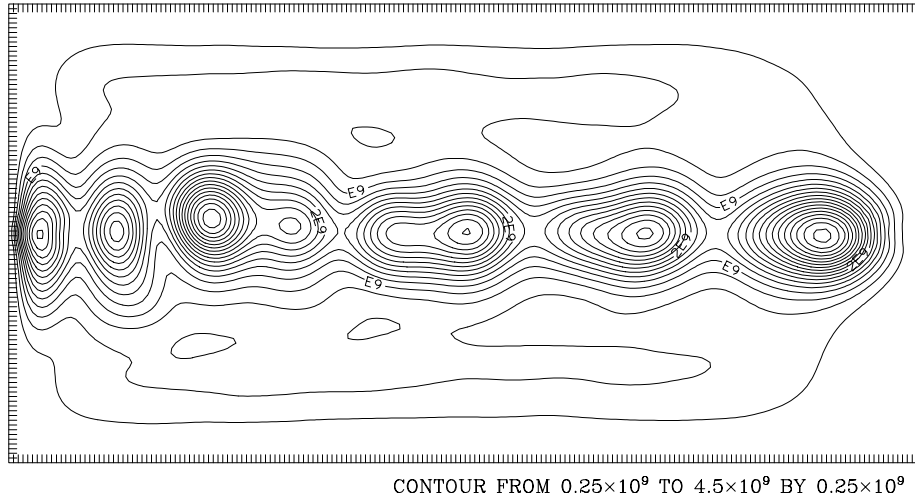
CONTOUR FROM 0.25×10⁹ TO 4.5×10⁹ BY 0.25×10⁹

Figure 3.25: $\overline{\psi' \cdot \psi'}$, note the series of Gaussian like features.

The most striking aspect of figure 3.25, is that to a first order approximation, it can be considered to be derived from Gaussian distributions. This result is also to a first order, what Hogg (1993) found in his analysis of the Gulf Stream. Further thought on the aspects of the $\overline{\psi' \cdot \psi'}$, would lead one to believe that this could be due to standing wave in the jet and while figure 3.9 of the mean streamfunction shows no obvious mean standing wave, the time mean of the standing wave would indeed vanish over a time integration of many periods of oscillation. However, traveling waves could not produce the Gaussian features in figure 3.25 as their mean eddy variance would be constant in the zonal direction. Thus we look to a plot of ψ along the y=0 line of the model (*i.e.* the center horizontal line of the model) versus time to picture the evolution of the axis of the jet which is shown in figure 3.26.
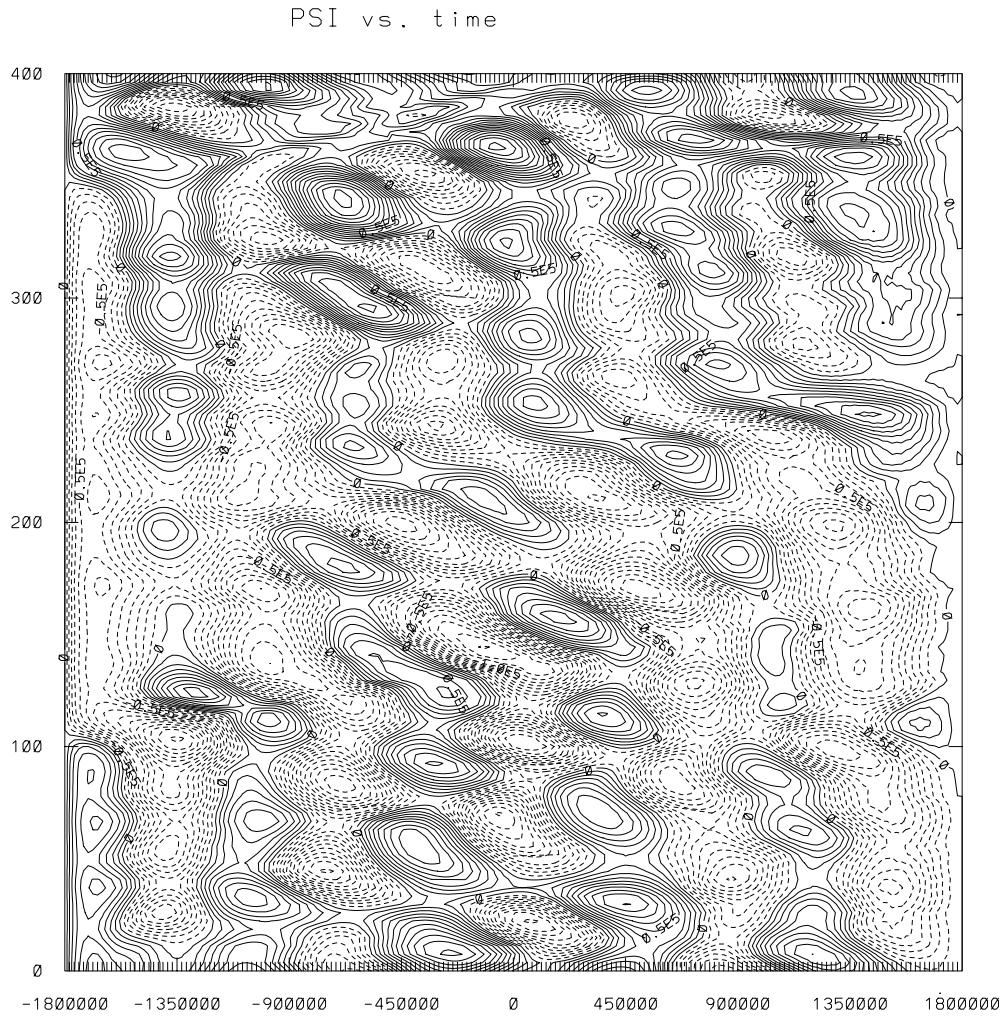
Figure 3.26: Contour plot of ψ vs. time for the last year of the model run, there appears to be both a standing mode and traveling mode to the wave pattern, zonal distance (in meters) is along the x-axis and time (in days) is along the y-axis.

The standing wave pattern seen in figure 3.26 can be idealized if we consider a time and space dependent streamfunction to be of the form:

$$\psi(x, y, t) = -(S)\,erf(\frac{y}{L} + \alpha\sin(kx)\sin(\sigma t)) \tag{3.8}$$

where S is the streamfunction strength, L is the jet half width, α is the amplitude of oscillation, k is the wave number and σ is the frequency of the standing wave. Once again considering equation 3.5 which states: $\overline{\psi' \cdot \psi'} = \overline{\psi \cdot \psi} - \overline{\psi} \cdot \overline{\psi}$, and knowing that the mean

36

streamfunction is of the form: $\bar{\psi} = -(S)\,erf(\frac{y}{L})$ gives us that:

$$\overline{\psi' \cdot \psi'} = \frac{1}{T}\int_0^T ((S)\,erf(\frac{y}{L}) + \alpha\sin(kx)\sin(\sigma t)))^2 dt - ((S)\,erf(\frac{y}{L}))^2 \tag{3.9}$$

While this is not a trivial integral to evaluate, some headway can be made on it by considering that it is a periodic function and therefore can be decomposed:

$$\overline{\psi' \cdot \psi'} = \frac{nS^2}{T}\int_0^{\frac{2\pi}{\sigma}} (erf(\frac{y}{L}) + \alpha\sin kx\sin\sigma t))^2 dt + \frac{S^2}{T}\int_{\frac{2n\pi}{\sigma}}^T (erf(\frac{y}{L}) + \alpha\sin kx\sin\sigma t))^2 dt - ((S)\,erf(\frac{y}{L}))^2 \tag{3.10}$$

Where n satisfies, $n = floor\,(\frac{\sigma T}{2\pi})$, the number of full oscillations made by the wave in the time T.

In the limit of: $T \gg \frac{2\pi}{\sigma}$, the last term is negligible and by substituting $\rho = \sigma t$ results in:

$$\overline{\psi' \cdot \psi'} = \frac{nS^2}{\sigma T}\int_0^{2\pi} (erf(\frac{y}{L}) + \alpha\sin kx\sin\rho))^2 d\rho - ((S)\,erf(\frac{y}{L}))^2 \tag{3.11}$$

We further make the approximation that for large T, $T \approx \frac{2n\pi}{\sigma}$ and therefore:

$$\overline{\psi' \cdot \psi'} = \frac{S^2}{2\pi}\int_0^{2\pi} (erf(\frac{y}{L}) + \alpha\sin kx\sin\rho))^2 d\rho - ((S)\,erf(\frac{y}{L}))^2 \tag{3.12}$$

While (3.12) is still not integrable, it is more tractable to numerical integration as it no longer depends on an unknown frequency of oscillation. To test this as a viable solution, we numerically integrated a simple case for set L, a and k. Our time dependant ψ is of the form in (3.7) and for $\rho=\pi/2$, the time of maximum amplitude, we obtain figure 3.27a and the time mean ψ is shown in figure 3.27b.
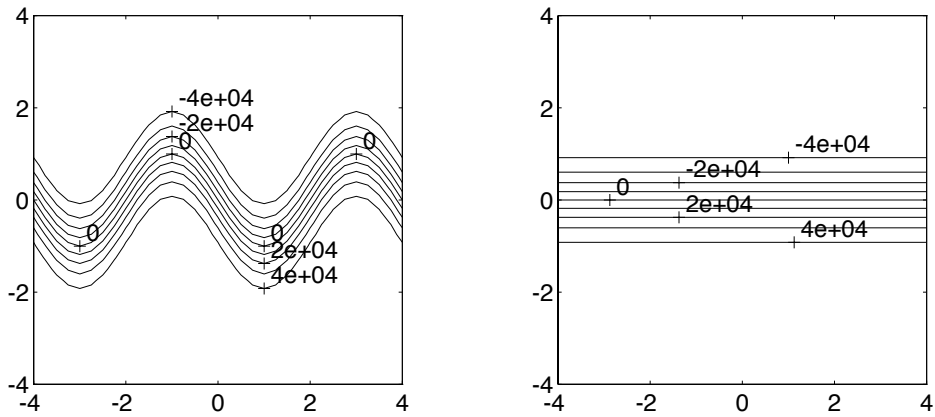
Figure 3.27: (a) ψ at maximum amplitude of oscillation, (b) time mean ψ

The numerical evaluation of the integral equation (3.12) for this case is shown in figure 3.28.
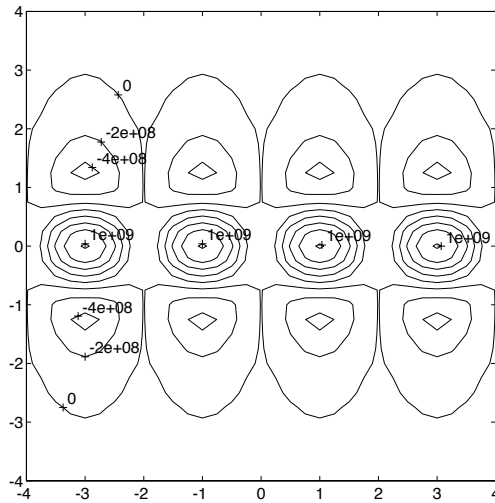

Figure 3.28: $\overline{\psi' \cdot \psi'}$ for (3.12)

Comparing figure 3.28 to figure 3.25, we can see that this approximation for the time dependant stream function is able to reproduce some gross features of the $\overline{\psi' \cdot \psi'}$ field indicating that a significant contribution to the pattern of figure 3.25 may come from a standing wave component. The separation between the centers of the $\overline{\psi' \cdot \psi'}$ features is $\frac{\pi}{k} = \frac{\lambda}{2}$, half the wavelength. In the next chapter we discuss what determines the wavelength of this standing wave.

Chapter 4

Parameter Variations

The major parameters of the model are the strength of the jet and the strength of the sponge layer. By varying these 2 parameters we were further able to grasp the dynamics of the model. First we varied the strength of the jet and found that for slower jets, the recirculation gyres became smaller in size and more numerous. For a streamfunction strength of 6250 m^2s^{-1}, maximum velocity of 0.135 m^2s^{-1}, the 10 year mean streamfunction is shown in figure 4.1. Note the numerous recirculation gyres, indicating a smaller wavelength for the standing wave.

New PSI at time   8000.

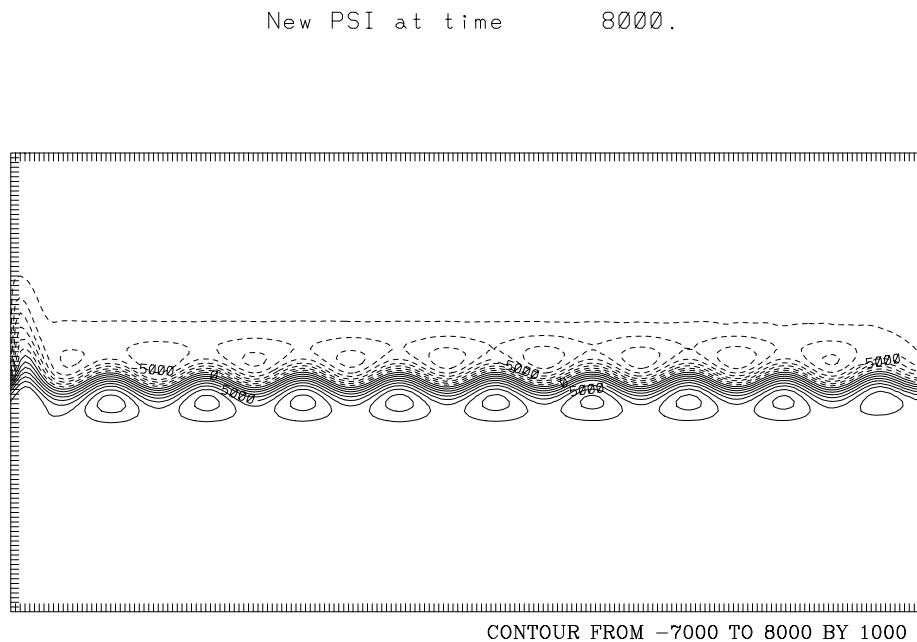CONTOUR FROM −7000 TO 8000 BY 1000

Figure 4.1: Mean streamfunction for slowest jet.

We quantified these results by measuring the spacing of the centers of the recirculation gyres. There was a distinct relationship between the speed of the jet and the wavelength of the recirculation gyres. The relationship was proportional to the square root of the jet speed in the following relation, as predicted by:

$$\lambda = 2\pi \left(\frac{u}{\beta}\right)^{1/2} \tag{4.1}$$

Equation (4.1) is the equation for a standing Rossby wave in a current of speed, u. Figure 4.2 summarizes this relation, compared with the model data.
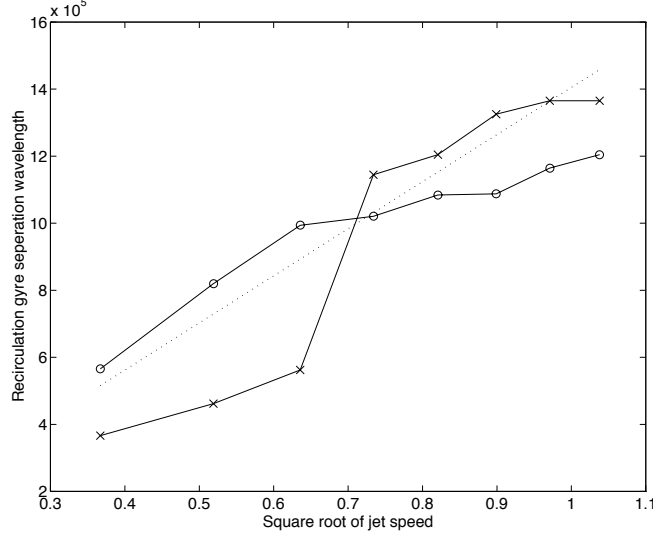

Figure 4.2: Summary of jet speed variations. 'x' indicate wavelength estimated from ψ mean fields and 'o' indicate estimates from the $\overline{\psi' \cdot \psi'}$ fields. The dotted line is the theoretical estimate from equation 4.1.

While the wavelength of the standing Rossby wave may the primary factor determining the wavelength of the $\overline{\psi' \cdot \psi'}$ features, there are clearly other factors affecting the wavelength of the meanders that develop. Intuitively, there is probably a strong quantization tendency from the finite model domain and specified boundary conditions.

The sponges in the model serve to absorb Rossby waves excited from the jet. Clearly their strength may have strong effects on the interior dynamics of the jet. This was, in fact, the case. From the plots of the cross-sections of $\overline{u' \cdot u'}$ and $\overline{v' \cdot v'}$ we estimated the e-folding scales for a $\overline{\psi'^2}$ of the form: $\sqrt{\overline{\psi'^2}} = Ce^{-\left(\frac{x}{L_x}\right)^2 - \left(\frac{y}{L_y}\right)^2}$, where L_x and L_y are the zonal and meridional e-folding scales respectively. We did this for jets with a streamfunction strength of 50000 m^2s^{-1} (maximum velocity of 1.078 ms^{-1}) and 25000 m^2s^{-1} (max

velocity of 0.539 ms^{-1}) over a variety of sponge strengths. There was a lower bound on the sponge strength set by stability of the model, sponges which were weaker than this limit allowed waves reflected off the wall to re-enter the interior of the model. When Rossby waves reflect off the western boundary, they reflect with a shorter wavelength. For weak sponges the reflecting Rossby waves will cause the model to become unstable since they are not adequately resolved by the grid spacing. Also, the transport of energy to the western boundary by the Rossby waves creates a western intensification by the rectification of the Rossby waves there. For sufficiently weak sponges this current enters the interior and contaminates the interior dynamics. Therefore there is an lower bound on the sponge strength. The zonal and meridional e-folding scales for 7 different sponge strengths are summarized in figures 4.3 and 4.4.
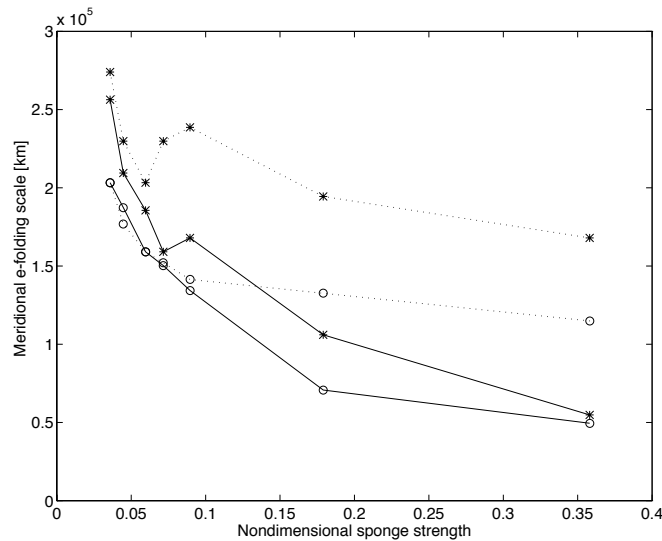

Figure 4.3: Estimates of the meridional e-folding scale, using a $50000\text{m}^2\text{s}^{-1}$ jet denoted by '*' and a $25000 \text{m}^2\text{s}^{-1}$ jet denoted by 'o'. Estimates from the $\overline{u' \cdot u'}$ are in solid lines, and estimates from the $\overline{v' \cdot v'}$ are the dotted lines.

The nondimensional sponge strength is defined as $A = \dfrac{L}{U\tau}$, where L is the half width of the jet, U is the maximum velocity of the jet and τ is the decay rate (in seconds) of the

sponges. In general we see a general decrease in the north-south e-folding scale with increasing sponge strength.
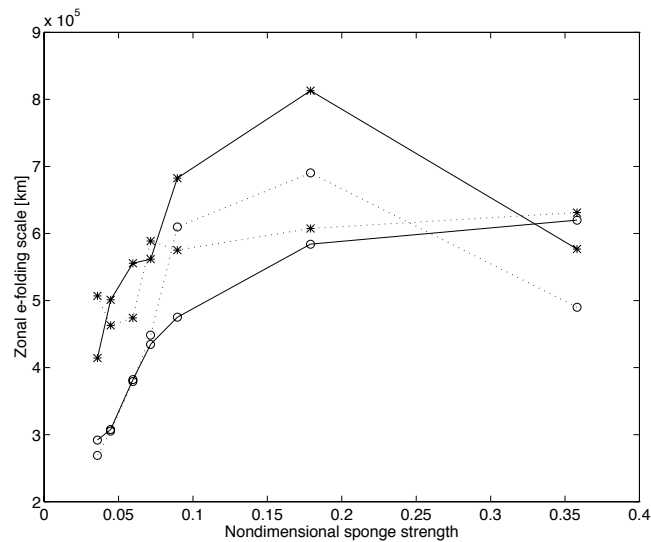

Figure 4.4: Estimates of the zonal e-folding scale, using a 50000m^{2}s^{-1} jet denoted by '*' and a 25000 m^{2}s^{-1} jet denoted by 'o'. Estimates from the $\overline{u' \cdot u'}$ are in solid lines, and estimates from the $\overline{v' \cdot v'}$ are the dotted lines.

The zonal scales show an opposite trend as the meridional scales. This situation can be explained by picturing the jet as a taut string with the sponges providing the tension. For stronger sponges the jet is stretched in the zonal direction, creating larger zonal scales, and in doing so can not meander as strongly, resulting in smaller meridional scales, and for weaker sponges the jet is less taut and therefore makes larger meanders.

Ideally the sponges would not influence the interior dynamics of the jet. However, the evolution of the jet is determined by waves which it is the sponges' job to absorb, therefore it is not a surprise that the sponges affect the dynamics of the jet.

42

Chapter 5

Results from the Barotropic Periodic Model

A zonally periodic code with and with out sponges was also run. The model parameters in these runs were the again the jet strength and jet half width, only they were applied as initial conditions instead of boundary conditions. We first show the results of a jet without the sponges. The jet is free to evolve as it chooses, however, there is nothing to cause a break in the symmetry of the basin and therefore a larger recirculation gyre on either side of the jet develops which slowly advects along the jet, and over time has a time mean of zero. This is the situation shown in figure 5.1.

New PSI at time 600000000.
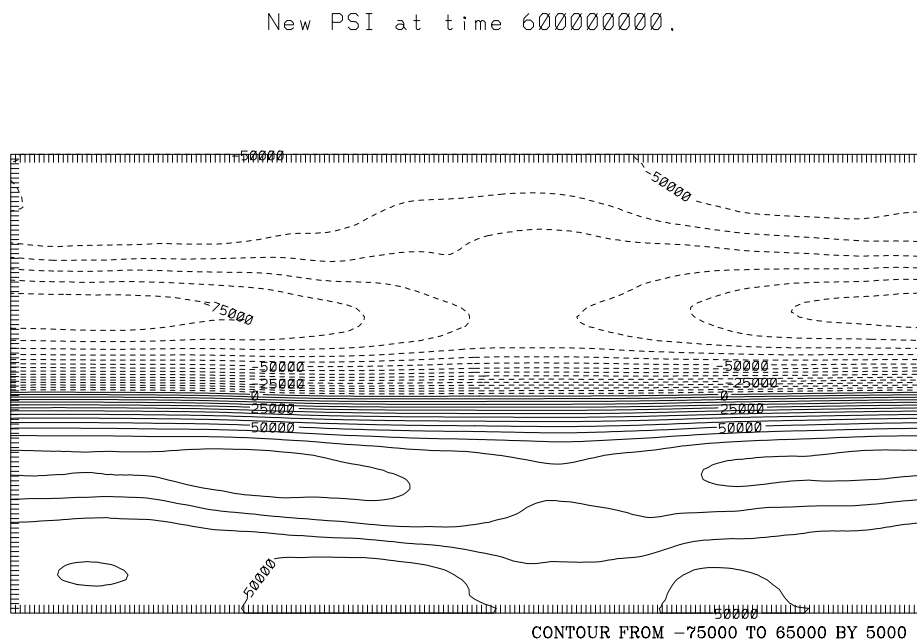

CONTOUR FROM -75000 TO 65000 BY 5000

Figure 5.1: Instantaneous ψ field from a zonally periodic model without sponges showing the development of two large gyres to either side of the jet.

The addition of sponges destroys the symmetry and the jet again begins meandering as seen in figure 5.2
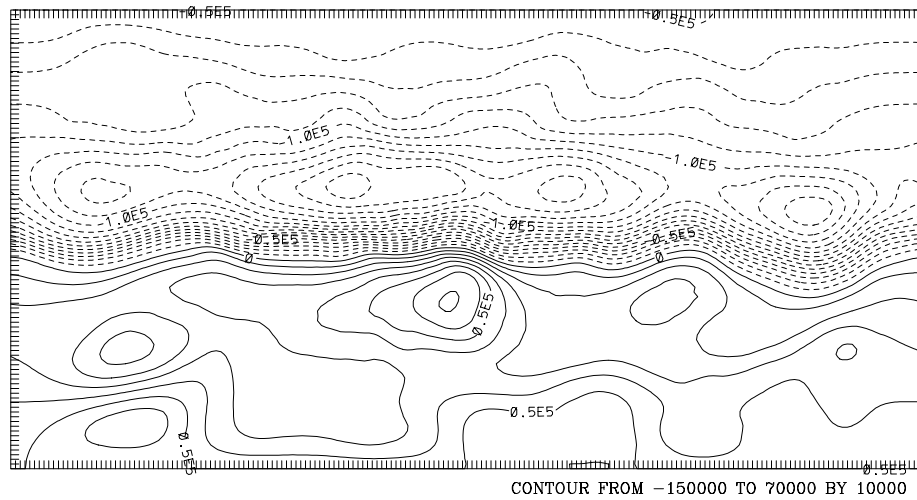
New PSI at time 600000000.

CONTOUR FROM -150000 TO 70000 BY 10000

Figure 5.2: Instaneous ψ field from a zonally periodic model with sponges showing a meandering jet

The time means for this jet are similar to those of the boundary condition jet described in previous chapters. Clearly the treatment of the boundaries plays an important role in the determination of the interior model dynamics. In the case with no sponges, the planet may as well be Jupiter with the development of large "Red Spot" like features. This points out the limitations of using a finite basin with unknown boundary conditions to describe the ocean with very complex boundaries. However, many of the dynamics of the jet are similar to observed jets in the ocean.

Chapter 6

Results from the Baroclinic Model

A two layer model was developed using the coupled quasi-geostrophic equations:

$$\left[\frac{\partial}{\partial t} + \frac{\partial}{\partial x}\psi_1\frac{\partial}{\partial y} + \frac{\partial}{\partial y}\psi_1\frac{\partial}{\partial x}\right] \times \left[\frac{\partial^2\psi_1}{\partial x^2} + \frac{\partial^2\psi_1}{\partial y^2} - F_1(\psi_1 - \psi_2) + \beta y\right] = 0 \qquad (6.1)$$

$$\left[\frac{\partial}{\partial t} + \frac{\partial}{\partial x}\psi_2\frac{\partial}{\partial y} + \frac{\partial}{\partial y}\psi_2\frac{\partial}{\partial x}\right] \times \left[\frac{\partial^2\psi_2}{\partial x^2} + \frac{\partial^2\psi_2}{\partial y^2} - F_2(\psi_2 - \psi_1) + \beta y\right] = 0 \qquad (6.2)$$

Where $\beta = 2.0 \times 10^{-11}\,(ms)^{-1}$, and F_1 and F_2 are defined as the inverse of the deformation radii of the layers, squared. $F_1 = (\frac{1}{40km})^2$ and $F_2 = (\frac{1}{90km})^2$. We took the upper layer depth to be 800 m and the lower depth to be 4200 m.

As in the one layer model, finite difference methods were used, the same time stepping routine was used, topography was neglected and dissipation was limited to two sponge layers at the eastern and western boundaries. The domain size and beta were the same as used in the barotropic model experiments. A jet was imposed as a boundary condition in the upper layer of the model, and lower layer was free to respond, but had $\psi = 0$ as its boundary conditions. The model tended toward the same behavior and for brevity we will simply show a instantaneous ψ plot after 20 years of time integration in figure 6.1.

New PSI at time 600000000.   Apr 08 1994 14:05:43

CONTOUR FROM -90000 TO 80000 BY 10000

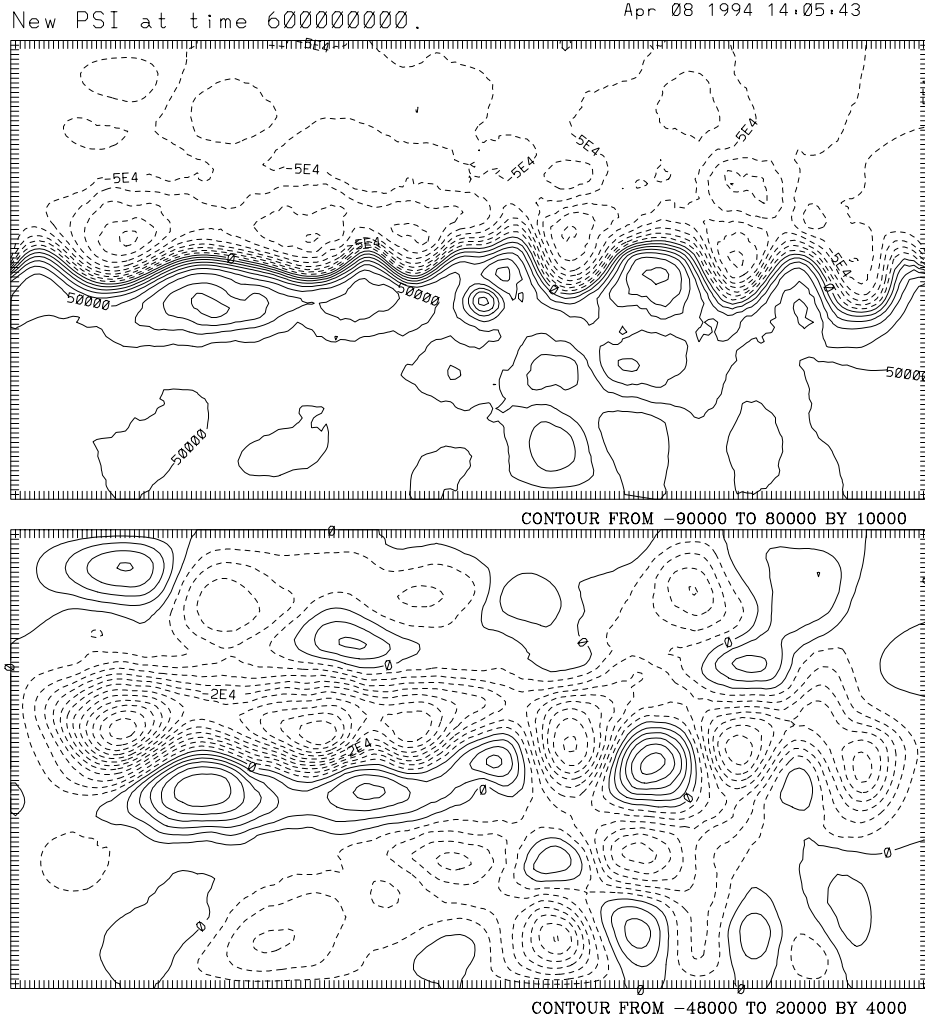CONTOUR FROM -48000 TO 20000 BY 4000

Figure 6.1: Result from 2 layer model, the upper layer is in the top frame and lower layer is in the bottom frame.

Of special note in figure 6.1, is the ring that has recently detached from the jet in the center of the upper layer. This is further confirmed in the plots of potential vorticity which show a circular feature at the same location. The time mean of the streamfunction seen in figure 6.2 shows that there is a mean recirculation along the jet in the upper layer, and that the lower layer of the model also responds with a recirculation, with the same sense as the upper layer. We calculate the transports from the mean streamfunction in each of the 2 layers of the model. In the upper layer there is a jet carrying 80 Sv. and each of the

recirculation gyres to the north and south carry an addtional 16 Sv. The lower layer's recirculation gyres each carry an additional 95 Sv. The 2 layer model has not been fully explored and will be subject of further study as it more accurately represents the case of a jet in the real ocean.
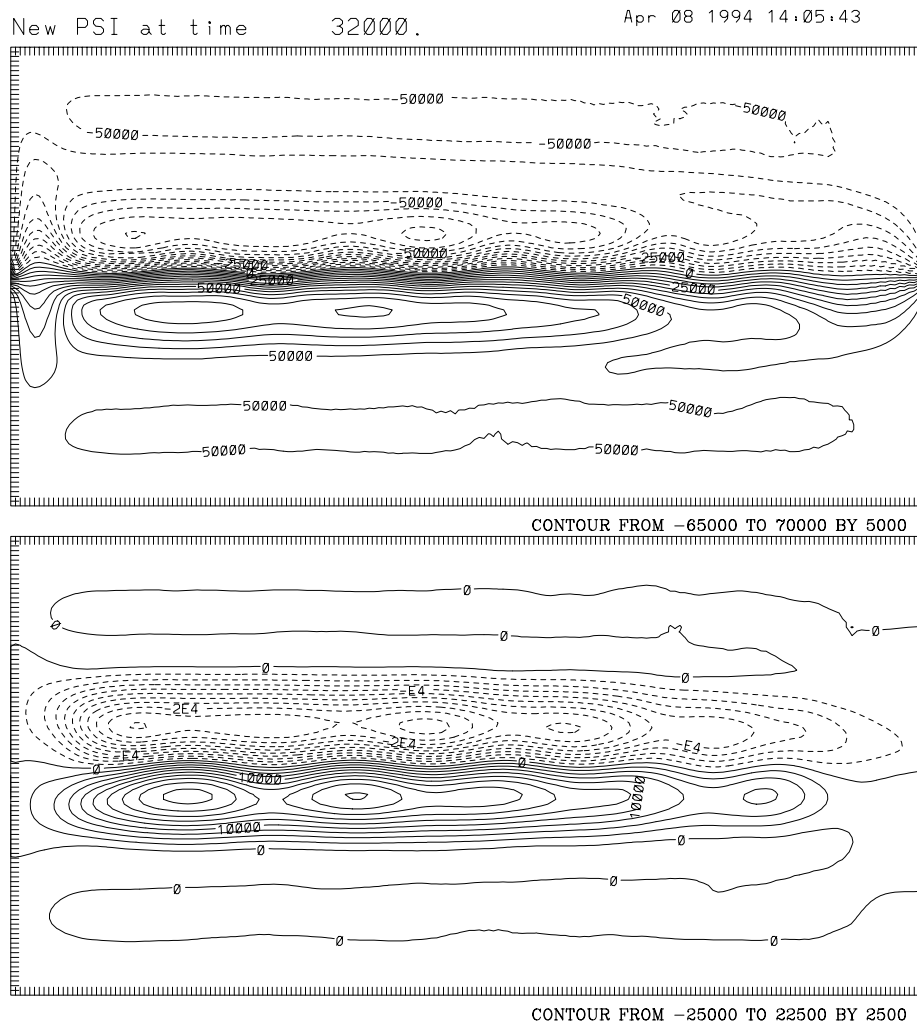
Figure 6.2: Mean streamfunction for 2 layer model showing counter-rotating recirculation gyres to north and south of the jet in both upper and lower layers.

Chapter 7

Conclusions

We have found that a simple model of a jet in the ocean can be dynamically very rich. The

jet meandered and forced large eddies to be produced. These eddies fluxed potential

vorticity and in the time mean, rectified to produce a mean recirculation current. The eddy

variance streamfunction can be idealized as Gaussian distributions resulting from standing

waves in the stream. The observed Reynolds' stress terms agree in morphology and within

an order of magnitude to the measured quantities from the model and Hogg's (1993)

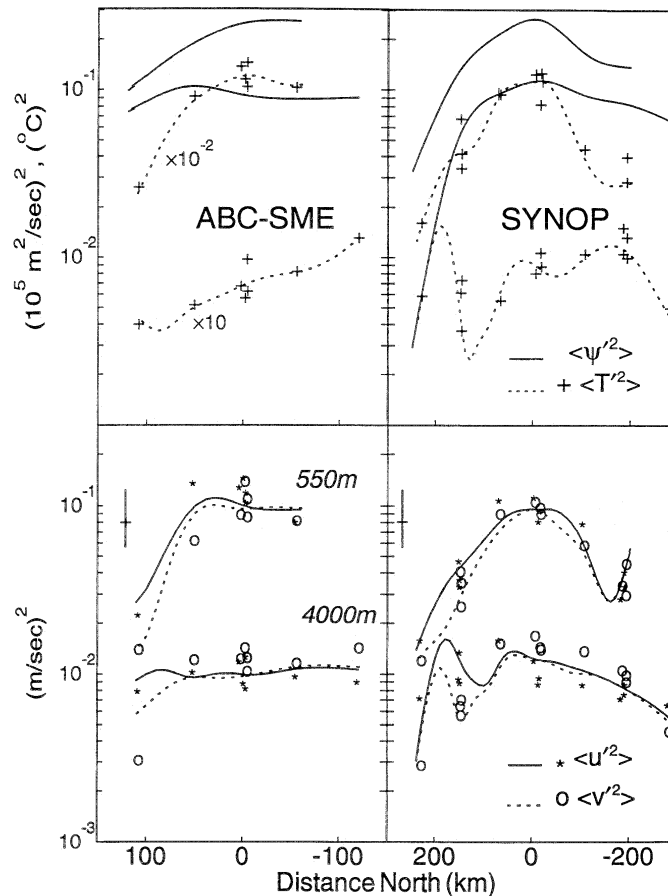observed values for the Gulf Stream.

Figure 7.1: Summary of results from Hogg, 1993. The measurements at the 550 m from the SYNOP and ABC-SME arrays agree in order of magnitude with our one layer model.

The barotropic model has been fully explored and its dynamics have been summarized here. The dynamics of our model resemble the results of Thompson and Schmitz (1989) for a flat bottomed model of the Gulf Stream with closed boundaries. The agreement between our simple model and the observed values (Hogg, 1993), as well as significantly more complex models is surprising. This leads us to believe that the forcing for the recirculation may in fact be a basic process, as we suggest, the flux of potential vorticity by eddies generated by the jet.

The baroclinic model, has not been investigated yet, and may hold more realistic dynamics in comparison to observations as we have done with the single layer model.

References

Adams, J., P. Swartztrauber and R. Sweet, 1988: FISHPAK; A package of FORTRAN subprograms for the solution of separable elliptic partial differential equations, version 3.2.

Arakawa, A., 1966: Computational Design for Long-Term Numerical Integration of the Equations of Fluid Motion: Two-Dimensional Incompressible Flow. Part 1. *Journal of Computational Physics*, **1**, 119-145.

Cessi, P., 1990: Recirculation and separation of boundary currents. *Journal of Marine Research*, **48**, 1-35.

Flierl, G. R., P. Malanotte-Rizzoli and N. J. Zabusky, 1987: Nonlinear waves and Coherent Vortex Structures in Barotropic Beta-plane Jets. *Journal of Physical Oceanography*, **17**, 1408-1438.

Haltiner, G. J. and R. T. Williams, 1980: Numerical Prediction and Dynamic Meteorology, second edition. John Wiley and Sons, New York, 477 pp.

Hogg, N. G., 1992: On the transport of the Gulf Stream between Cape Hatteras and the Grand Banks. *Deep-Sea Research*, **39**, 1231-1246.

Hogg, N. G., 1993: Toward parameterization of the eddy field near the Gulf Stream. *Deep-Sea Research*, **40**, 2359-2376.

Holland, W. R. and P. B. Rhines, 1980: An example of Eddy-Induced Ocean Circulation. *Journal of Physical Oceanography*, **10**, 1010-1031.

Holland, W. R., T. Keffer and P. B. Rhines, 1984: Dynamics of the oceanic general circulation: the potential vorticity field. *Nature*, **308**, 698-705.

Malanotte-Rizzoli, P., N. G. Hogg and R. E. Young, submitted: Stochastic Wave Radiation by the Gulf Stream: Numerical Experiments. *Deep-Sea Research*.

Thompson, J. D. and W. J. Schmitz, 1989: A Limited-Area Model of the Gulf Stream: Design, Initial and Model-Data Intercomparison. *Journal of Physical Oceanography*, **19**, 791-814.